Augmented Incremental Potential Contact for Sticky Interactions

Yu Fang*, Minchen Li*, Yadi Cao, Xuan Li, Joshuah Wolper, Yin Yang, and Chenfanfu Jiang

Abstract—We introduce a variational formulation for simulating sticky interactions between elastoplastic solids. Our method brings a wider range of material behaviors into the reach of the Incremental Potential Contact (IPC) solver recently developed by [1]. Extending IPC requires several contributions. We first augment IPC with the classical Raous-Cangemi-Cocou (RCC) adhesion model. This allows us to robustly simulate the sticky interactions between arbitrary codimensional-0, 1, and 2 geometries. To enable user-friendly practical adoptions of our method, we further introduce a physically parametrized, easily controllable normal adhesion formulation based on the *unsigned distance*, which is fully compatible with IPC's barrier formulation. Furthermore, we propose a smoothly clamped tangential adhesion model that naturally models intricate behaviors including debonding. Lastly, we perform benchmark studies comparing our method with the classical models as well as real-world experimental results to demonstrate the efficacy of our method.

Index Terms—Physically Based Animation, Optimization Time Integration

1 Introduction

Simulating frictional contact on solids has been a trending research direction in computer animation for many years [2], [3], [4], yet much less attention has been paid to adhesion, a closely-related mechanism. Adhesive objects are ubiquitous, such as tape, candy, jello, rice, sticky toys, etc.

A state-of-the-art work for solid adhesion in computer graphics was performed by [5]. Based on the Raous, Cangemi, Cocou (RCC) adhesion model [6], [5] formulated a mixed linear complementarity problem (MLCP) to cover contact, friction, and adhesion constraints, and they solve the problem with the Projected Gauss-Seidel (PGS) method. LCP and PGS constraint dynamics solvers are widely used in graphics and achieved great success, but they typically could not guarantee interpenetration-free results. Adhesion is an intricate effect on the interface between materials in contact. If a method permits intersections, the boundaries of the materials will be dislocated, and the interface will disappear, making adhesion ill-defined and impossible to be captured properly. For instance, our Taping Armadillo example (Figure 1, right), which involves codimensional geometries and large deformations, is a typical case that challenges methods without non-penetration guarantees.

More recently, [1] proposed Incremental Potential Contact (IPC), a variational, Newton-based nonlinear frictional contact solver. Unlike previous approaches, their method guarantees solver convergence and interpenetration-free geometric states throughout the entire simulation for arbitrarily large timestep sizes and extreme deformations. Correspondingly, extending the IPC formulation with adhesion will further improve its versatility and widen its impact.

We thus augment IPC with the RCC adhesion model to enable robust and controllable simulation of sticky materials in arbitrary codimensional geometries and deformation with guaranteed non-interpenetration. However, directly applying RCC can immediately introduce six additional parameters to be tuned for capturing realistic adhesion effects. Furthermore, RCC models adhesion intensity at the contact regions with another set of variables to be evolved through time, which is challenging to deal with in optimization time integrators.

To avoid treating adhesion intensity as a separate variable, we further propose energetically consistent models for the adhesion force. In particular, we keep the unsigned distance as the primary variable and propose a physically intuitive and user-friendly model for normal adhesion. This provides an adhesion force-distance curve well-matching that of the RCC model. On the other hand, correctly simulating tangential adhesion is also of great importance for modeling realistic debonding behaviors. Unlike the normal force, tangential adhesion is by nature non-integrable and does not have a variational form. Inspired by IPC's friction model, we propose an integrable semi-implicit tangential adhesion model that can converge to the implicit solution through iterative tangent basis updates. Analogous to the normal component, without introducing an additional adhesion intensity variable, our tangential adhesion force-displacement curve well-matches that of the RCC model.

Our adhesion model can be conveniently incorporated into an existing IPC-based contact solver, with only two additional parameters introduced for independent control of the normal and tangential adhesion stiffness. By analyzing the adhesion model as linear elasticity, we reparameterize the adhesion stiffness into the Pascal unit. This permits us to correlate it with the Young's modulus of the elastic material, thereby facilitating a more intuitive configuration of parameters. Due to the usage of the filter-line-search scheme and smooth potentials, the resulting simulation is guaranteed to converge without any interpenetration even with large timestep sizes.

To summarize, our contributions include:

• **Joint first authors. Y. Fang and J. Wolper are with the University of Pennsylvania; M. Li is with Carnegie Mellon University; Y. Yang is with the University of Utah; Y. Fang, M. Li, Y. Cao, X. Li, and C. Jiang are (also) with the University of California, Los Angeles. E-mail: (Minchen Li) minchernl@gmail.com, (Chenfanfu Jiang) cffjiang@math.ucla.edu.*

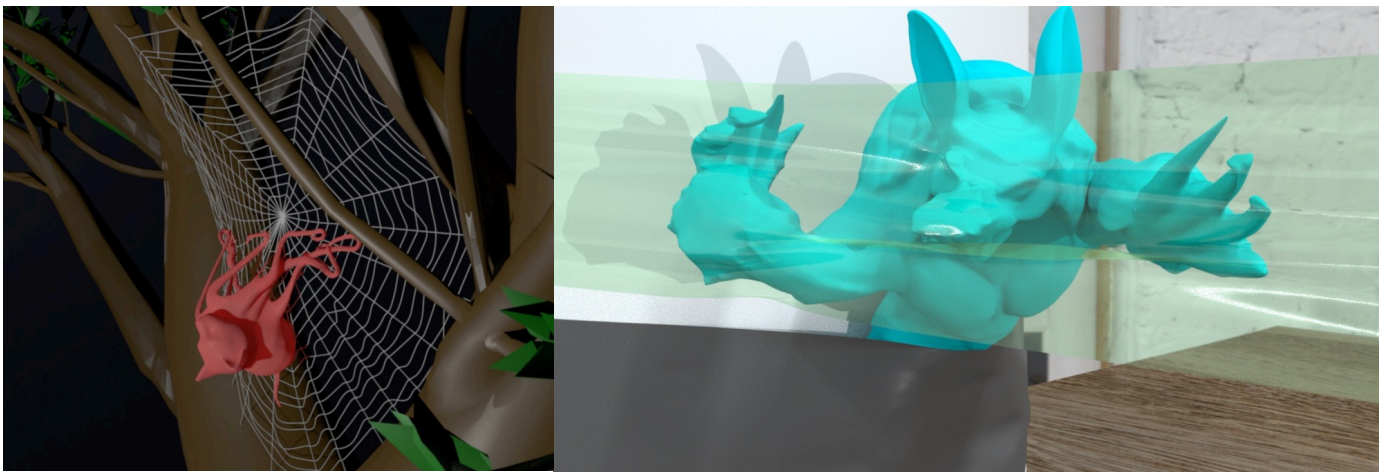

Fig. 1. **Spider Web and Tape.** Extending the Incremental Potential Contact variational framework allows us to robustly simulate complex scenes with mixed-dimensional geometry and deforming and contacting bodies with versatile friction and adhesive behaviors. The **left** simulation shows an octocat hanging on a sticky spider web upside down, and the **right** simulation demonstrates the process of slowly peeling a strip of adhesive tape off the armadillo attached to a pillar. Both are simulated with guaranteed stability and non-penetration even with large deformation and time step sizes.

- A distance-based variational adhesive contact model that is compatible with primal Newton Barrier time integrators;
- An iterative stress tangential adhesion model that reproduces realistic debonding behaviors;
- An augmented Incremental Potential Contact framework for unified and controllable animation of contact, friction and adhesion.

We demonstrate the efficacy of our method with various benchmark experiments and challenging examples spanning rods, shells, and volumes with large deformation.

2 Related Work

2.1 Adhesion Modeling

The interaction between ideal surfaces that are molecularly smooth and undamaged is well understood in both theories and experiments. Nonetheless, in most practical scenarios, surfaces are rough and so exhibit complicated tribological behaviors including adhesion, friction, and lubrication [8]. Predicting the interactions of rough materials remains an open challenge.

There are several mature models for adhesion on ideal surfaces. For example, the Johnson, Kendall, Roberts (JKR) model [9], the Derjagin, Muller, Toropov (DMT) model [10], the Lennard-Jones (LJ) model [11], etc. These models are mainly based on single sphere contact, and only a few others model real-world rough surfaces either as a collection of asperities [12], or as a nominally flat surface embedded by nonplanarity [13]. Despite these improvements, the above models still require ultra-smooth surfaces with asperity deviation of nanometers.

A famous model for the real-world, macroscopic adhesion-friction interaction is the Raous, Cangemi, Cocou (RCC) model [6]. In RCC, the adhesion intensity is characterized by the bonding and debonding process, i.e., the intensity varies not only with displacement, but also with the time elapsed in the process, and it is strongly coupled with the Coulomb friction force. Recently, [14] proposed an improved bi-potential model based on RCC, and this model was later optimized explicitly for orthotropic surfaces [15].

In computer graphics, although many works investigated adhesion modeling at solid-fluid interfaces [16], [17], [18], [19], [20], [21], [22], [23], there have been notably fewer studies focused on capturing the sticky interactions between deformable solids. In particular, [5] formulated a mixed linear complementarity problem (MLCP) to incorporate the RCC model for simulating adhesive contact. This method was later applied by [24] to capture the adhesion between sticky lips. Despite the difficulties in accurately predicting adhesive interactions in real-world scenarios, these works in computer graphics demonstrate that it is still practical to take inspiration from classical models, e.g., RCC, to produce realistic visual effects.

We apply the RCC model to augment the Incremental Potential Contact (IPC) framework with adhesion. By directly approximating the constitutive behaviors between adhesion forces and displacements, we avoid evolving the adhesion intensity as a separate variable and obviate the need for inequality constraints.

2.2 Barrier-based Contact

Barrier methods are important tools to handle inequality constraints [25]. They are also one of the standard options for handling the non-interpenetration constraints in contact mechanics [26], [27], [28]. In physics-based animation, [29] modeled the interactions between threads with a barrier method to simulate cloth at yarn level; [30] designed a contact barrier with an infinite sum of nested quadratic potentials for reliably simulating elastica in complex contact scenarios with explicit time integration.

Our new adhesion model is based on the Incremental Potential Contact (IPC) method [1], where the non-penetration constraints are novelly formulated using precisely calculated unsigned distances between boundary elements, and

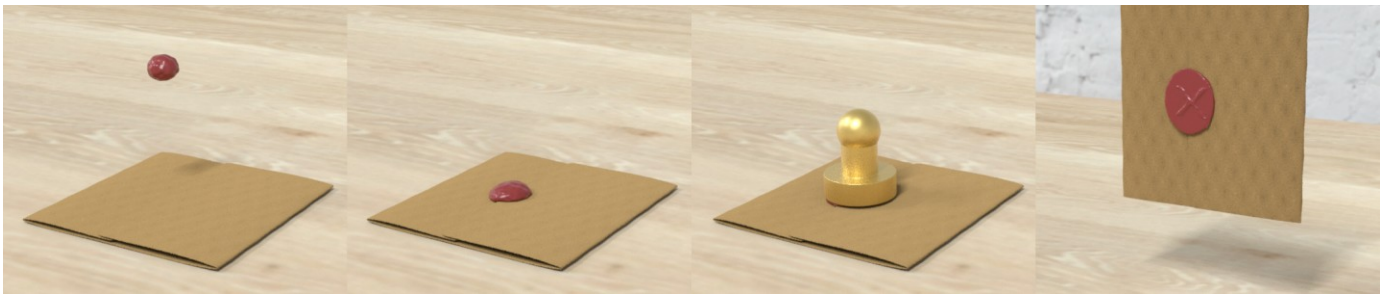

Fig. 2. **Wax seal.** Our distance-based model is robust under severe compression and large plastic deformations. Here, we press on top of a small dollop of wax to seal the letter. The wax remains adhesive after being squashed and is printed with an 'X' mark by the stamp. The wax is modeled with an energetically consistent von-Mises plasticity with StVK elasticity [7] within our optimization time integrator.

a smoothly clamped barrier function is applied to enforce these constraints. Together with a filter-line-search scheme based on continuous collision detection (CCD), IPC guarantees global convergence and non-penetration for solids with arbitrary codimensional geometries [31] and deformation. More subsequent works have shown the formulation's versatility towards solving problems in reduced simulation of deformable [32] and rigid objects [33], [34], articulated multibody dynamics [35], projective dynamics [36], simulating viscoelastic and elastoplastic solids [7], frictional contact between embedded interfaces [37], and coupling between different spatial discretizations [38], [39]. In addition to physical simulations, barrier methods were also adopted in geometry processing to guarantee injectivity. [40] employed barrier energies to guarantee inversion-free in shape deformation and mesh parameterization problems. [41] and [42] applied barrier methods to further guarantee non-overlap on the UV map during mesh parameterization. Based on IPC, [43] proposed the Injective Deformation Processing (IDP) framework to robustly solve mesh deformation problems while enforcing global injectivity.

3 Background

3.1 Incremental Potential Contact (IPC)

In IPC [1], the dynamic simulation of elastic solids with frictional contact is achieved by solving a nonlinear optimization problem

$$\mathbf{x}^{n+1} = \arg\min_{\mathbf{x}} \left(\frac{1}{2}\|\mathbf{x} - \tilde{\mathbf{x}}^n\|^2_{\mathbf{M}} + \beta h^2 \sum_i P_i(\mathbf{x}) \right) \tag{1}$$

in each time step n for the new nodal position $\mathbf{x}^{n+1}$, followed by updating velocity $\mathbf{v}$ according to the applied time integration rule. Here $\mathbf{M}$ is the mass matrix; h is the time step size; and $P_i(x)$ are the potential energies for gravity, elasticity, contact, and friction, etc. $\tilde{\mathbf{x}}^n$ and β both depend on the time integration rule. For example, with implicit Euler, $\mathbf{v}^{n+1} = (\mathbf{x}^{n+1} - \mathbf{x}^n)/h$, $\tilde{\mathbf{x}}^n = \mathbf{x}^n + h\mathbf{v}^n$, $\beta = 1$. The objective function of this optimization problem is called the Incremental Potential [44], [45].

IPC rigorously formulated the non-interpenetration constraints using precisely calculated unsigned distance d_k between all non-adjacent boundary element pairs, k. These distances are required to remain positive throughout the optimization in every timestep, which is achieved by applying a barrier energy $P_b(\mathbf{x}) = \sum_k w_k b(d_k)$ with area weight w_k and energy density function

$$b(d) = \begin{cases} -\kappa_b \hat{d}_b (\frac{d}{\hat{d}_b} - 1)^2 \ln(\frac{d}{\hat{d}_b}) & 0 < d < \hat{d}_b \\ 0 & d \geq \hat{d}_b \end{cases} \tag{2}$$

in the Incremental Potential. Here κ_b is the contact stiffness and $\hat{d}_b$ is a distance threshold below which contact forces are exerted. Note that $b(d)$ is at least C^2-continuous everywhere even at $d = \hat{d}_b$. As $d \to 0$, we have $b(d) \to \infty$ (Figure 7, blue curve), providing arbitrarily large repulsion to avoid interpenetration. Together with a filter-line-search scheme based on continuous collision detection (CCD), IPC guarantees global convergence and non-interpenetration even under conditions of substantial deformation or high-speed impacts. When $\hat{d}_b \to 0$, the IPC model converges to the non-smooth contact model.

In the tangent direction, IPC also models friction with an approximated smooth potential energy $P_f(\mathbf{x})$. At contact pair k, a mollified Coulomb friction force is defined as

$$\mathbf{t}_f = \mu \lambda_k f_1(\|\mathbf{u}_k\|) \frac{-\mathbf{u}_k}{\|\mathbf{u}_k\|}, \tag{3}$$

where μ is the friction coefficient, λ_k is the normal contact force magnitude at contact pair k, $\mathbf{u}_k = T_k(\mathbf{x})^T(\mathbf{x} - \mathbf{x}^n)$ is the tangent relative sliding displacement with the tangent operator $T_k(\mathbf{x})$, and $f_1(y)$ is a continuous function to mollify the stick-slip transition (Figure 9, blue curve)

$$f_1(y) = \begin{cases} -\frac{y^2}{\epsilon_v^2 h^2} + \frac{2y}{\epsilon_v h} & 0 < y < \epsilon_v h \\ 1 & y \geq \epsilon_v h. \end{cases} \tag{4}$$

Here ϵ_v is the velocity threshold below which static friction force is applied. With λ and T temporally fixed as $\hat{\lambda}$ and $\hat{T}$ during the nonlinear optimization (Equation 1), $P_f(\mathbf{x}) = \sum_k \mu \hat{\lambda}_k f_0(\|\hat{\mathbf{u}}_k\|)$ with $f_0'(y) = f_1(y)$ and $\hat{\mathbf{u}}_k = \hat{T}_k^T(\mathbf{x} - \mathbf{x}^n)$ is a well-defined potential energy whose negative gradient generates the mollified semi-implicit friction force [1]. Through an outer loop of fixed-point iterations which alternates between the nonlinear optimization and the update of $\hat{\lambda}$ and $\hat{T}$, IPC converges to the solution with fully implicit friction.

3.2 The Raous-Cangemi-Cocou (RCC) Adhesion Model

Here we introduce the RCC model [6] applied in [5]. In terms of displacements, both the normal and tangential RCC

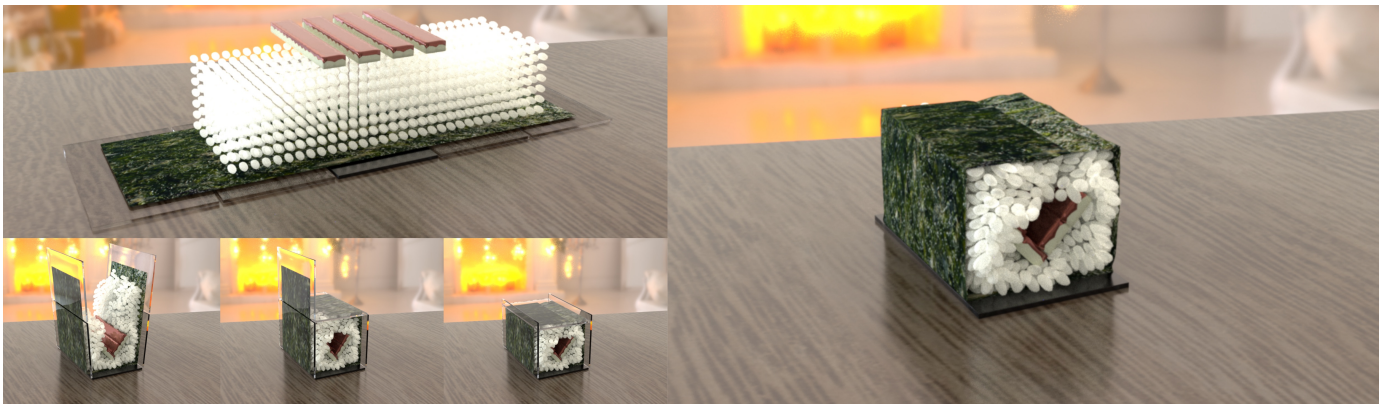

Fig. 3. **Making Sushi.** We create our unique sushi machine by scripting the movement of five plates. Nori, rice, and the inner chocolate bars, whether volumetric or condimensional, all stick together with consistently resolved adhesion behaviors.

models are quadratic energies. The intricate behaviors are modeled along with another set of simulation degrees-of-freedom – the adhesion intensity.

3.2.1 Normal Adhesion

The normal adhesion energy density per unit area at contact pair k is defined as

$$P_{N,k} = \frac{C_N}{2}\beta_k^2 d_k^2, \tag{5}$$

where C_N is the constant normal adhesion stiffness, $\beta_k \in [0,1]$ is the adhesion intensity at contact pair k, and d_k is the distance. Integrating the energy density over contact regions, we obtain the normal adhesion potential energy $P_N(\mathbf{x}) = \sum_k w_k P_{N,k}$ with w_k being the area weight.

3.2.2 Tangential Adhesion

Similarly, the tangential adhesion energy density at contact pair k is defined as

$$P_{T,k} = \frac{C_T}{2}\beta_k^2 \|\mathbf{u}_k\|^2, \tag{6}$$

where C_T is the constant tangential adhesion stiffness and $\mathbf{u}_k$ is the relative sliding displacement at contact pair k. The tangential adhesion potential energy is defined as $P_T(\mathbf{x}) = \sum_k w_k P_{T,k}$.

3.2.3 Adhesion Intensity

In [5], the adhesion intensity β_k is fixed per timestep, and evolved separately from the main degree-of-freedom before each timestep via explicit Euler

$$\beta_k^{n+1} = \min(1, \max(0, \beta_k^n + h\dot{\beta}_k^n)), \tag{7}$$

where $\dot{\beta}_k$ is the varying speed of β_k depending on the contact configurations.

Let p_k be the total normal pressure at contact pair k. When $p_k < 0$ (adhesion is active), debonding is triggered, and with linear approximation to the RCC model,

$$\dot{\beta}_k = \frac{1}{\eta}\min(W - C_N\beta_k d_k^2 - C_T\beta_k\|\mathbf{u}_k\|^2, 0), \tag{8}$$

where η is a viscosity parameter, and W is a maximum adhesion energy. When $p_k > 0$ (non-penetration constraint is active), the normal motion triggers bonding, but any tangential motion still results in debonding, thus we have

$$\dot{\beta}_k = r\max(p_k - \beta_k p_0, 0) + \frac{1}{\eta}\min(W - C_T\beta_k\|\mathbf{u}_k\|^2, 0), \tag{9}$$

where r is the bonding rate, and p_0 is a compression value for saturation.

Now we can see that the RCC model introduces six parameters (C_N, C_T, η, W, r, p_0) to the simulation. The last four parameters that determine $\dot{\beta}$ indirectly model the constitutive behavior between adhesion forces and displacements during bonding and debonding (see Figure 5 and Figure 9). It is up to future research to assess if they are effective for capturing complicated behaviors, although they could still complicate the simulation setup for the majority of adhesion effects.

4 Method

To augment IPC with the RCC adhesion model while avoiding treating adhesion intensity as another set of degrees-of-freedom, we directly model the constitutive relation between adhesion forces and displacements to approximate results from RCC.

We start by examining the force-displacement curve of the RCC model given by [6]. In a 2D case, with complete adhesion ($\beta = 1$) and zero displacement initially, we first analyze the normal behavior (Figure 5, right). Under compression, the non-interpenetration constraint is strictly enforced, while under traction, an adhesive resistance is active, causing the adhesion force to increase with the displacement. Next, the intensity of adhesion starts to decrease when the displacement is sufficiently large such that the adhesion energy exceeds the limit W (Equation 9). When adhesion is totally broken, the adhesion force decreases to 0. The tangential adhesion follows a very similar pattern (Figure 9, left). Our idea is to augment both the barrier and friction energy by incorporating an additional term that provides a similar adhesion force-displacement relation as observed above.

4.1 Augmented IPC Barrier for Normal Adhesion

Let $0 < \hat{d}_b \leq \hat{d}_p < \hat{d}_a$ be a sequence of distance thresholds where the IPC barrier energy density $b(d)$ is active on $(0, \hat{d}_b)$

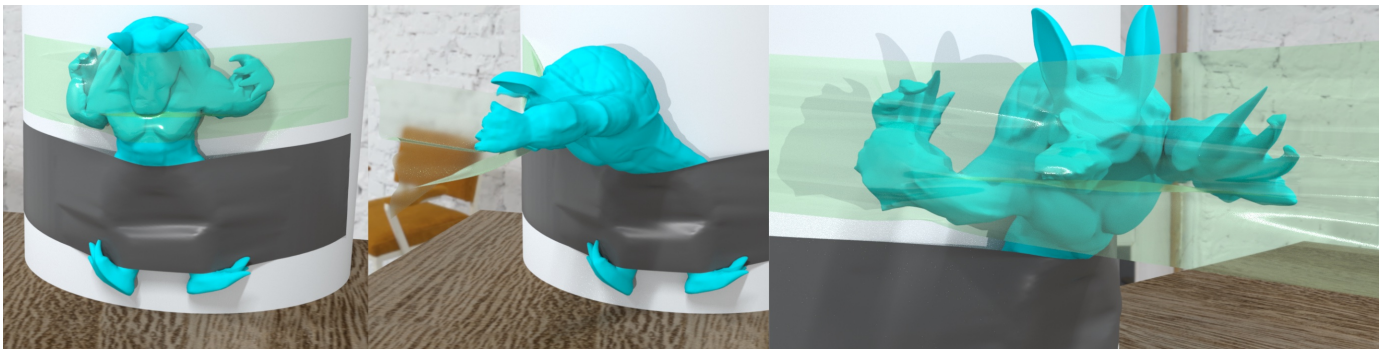

Fig. 4. **Taping Armadillo.** An elastic armadillo is attached to a pillar by two strips of adhesive tape. As we slowly peel away one of the strips, the armadillo's face and hands reluctantly go through debonding and exhibit intricate, sticky deformations during the process.

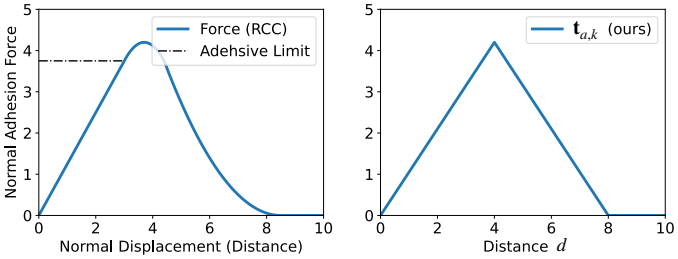

Fig. 5. **RCC v.s. Our Normal Adhesion.** Our model approximates the RCC force-displacement relation using piecewise linear functions.

to avoid interpenetration. We design our adhesion energy density $a(d)$ to be active on $(0, \hat{d}_a)$, and let it reach the steepest (corresponding to the largest adhesion force) at $\hat{d}_p$. To achieve this, we define $a(d)$ as a piecewise quadratic function

$$a(d) = \begin{cases} a_1 d^2 + c_1 & 0 < d < \hat{d}_p \\ a_2 d^2 + b_2 d + c_2 & \hat{d}_p \le d < \hat{d}_a \\ 0 & d \ge \hat{d}_a, \end{cases} \tag{10}$$

where $a_1 = a_2(1 - \frac{\hat{d}_a}{\hat{d}_p})$, $c_1 = a_2(\hat{d}_a - \hat{d}_p)^2 - \hat{d}_p^2 a_1$, $b_2 = -2a_2\hat{d}_a$, $c_2 = a_2\hat{d}_a^2$, and $a_2 < 0$ is an adjustable parameter relating to the maximum derivative of a, namely $2a_2(\hat{d}_p - \hat{d}_a)$ at $d = \hat{d}_p$. Note that by our construction, $a'(0) = a(\hat{d}_a) = a'(\hat{d}_a) = 0$, and $a(d)$ is at least C^1-continuous everywhere (Figure 7, right, orange curve). In this way, our adhesion-distance relation is consistent with the RCC model that the force increases from 0 until reaches a peak and then decreases back to 0 as distance increases. Then, we can augment the IPC energy density function with the adhesion term and obtain $b(d) + a(d)$, which captures both contact and adhesion (Figure 7, left, yellow curve). The augmented energy first smoothly decreases from 0 to a local minimum for adhesion as the distance gets below $\hat{d}_a$, and then increases to infinity as the distance approaches 0.

By integrating the augmented IPC energy density on the boundary of the solids , we obtain the normal-component adhesive contact potential $P_N(\mathbf{x}) = \sum_k w_k(b(d_k) + a(d_k))$. The potential energy on each contact pair is properly weighted with the estimated contact area, which is consistent across resolutions.

4.2 Strength of Normal Adhesion

To reparameterize the adjustable parameter a_2 to a material-related quantity for more convenient experimental setup, we analyze the pressure balance between adhesion and elasticity at the contacting areas.

Similar to the normal force magnitude λ in IPC friction, the normal adhesion pressure at contact pair k can be computed as $-\frac{\partial a}{\partial d}(d_k)$, which measures the normal adhesion force magnitude per unit area. Now consider a linear elastic material with Young's modulus Y sticking on the ground (no gravity). If we set a_2 such that

$$-\frac{\partial a}{\partial d}(\hat{d}_p) = -Y\varepsilon_c, \tag{11}$$

which implies the maximum pressure of normal adhesion is only able to balance the stress of the material up to strain ε_c, after slowly pulling the material away from the ground, it will be fully detached once it deforms uniformly with a strain measure ε_c near the sticking area. Essentially, stress is also a pressure quantity that measures the elastic force per unit area. Therefore, when the solid deforms more and stress increases further, exceeding the maximum pressure of adhesion, detachment must happen. Solving Equation 11 gives us

$$a_2 = \frac{Y\varepsilon_c}{2(\hat{d}_p - \hat{d}_a)}. \tag{12}$$

The detachment stress can be independent of Young's modulus; by reusing Y from the solid material property, we can intuitively set ε_c to achieve the desired adhesion behaviors. We use the smaller Y for contacting objects with different Young's modulus. As for the distance thresholds, we can practically set them relative to the IPC active distance $\hat{d}_b$: $\hat{d}_p = \hat{d}_b$ and $\hat{d}_a = 2\hat{d}_b$.

4.3 Tangential Adhesion

Inspired by IPC friction, we define our tangential adhesion force at contact pair k as

$$\mathbf{t}_{a,k} = \mu_a \lambda_{a,k} f_t(\|\mathbf{u}_k\|) \frac{-\mathbf{u}_k}{\|\mathbf{u}_k\|}, \tag{13}$$

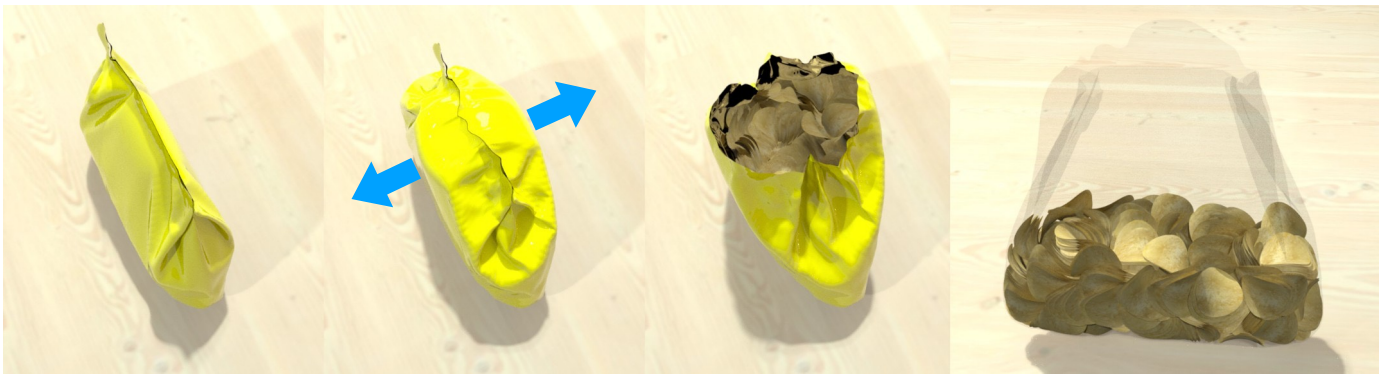

Fig. 6. **Opening Chips Bag.** A bag containing 750 chips is sealed with adhesion. We show the process of pulling the bag slowly on the top until it is opened. Here, intricate frictional contacts between the chips are also realistically captured.

where $\mu_a \geq 0$ is an adjustable tangential adhesion coefficient similar to the friction coefficient, $\lambda_{a,k}$ is the maximum possible value of normal adhesion force magnitude at contact pair k, and $f_t(y)$ is a continuously clamped quadratic function:

$$f_t(y) = \begin{cases} -\frac{y^2}{\epsilon_a^2 h^2} + \frac{2y}{\epsilon_a h} & 0 < y < 2\epsilon_v h \\ 0 & y \geq 2\epsilon_v h. \end{cases} \tag{14}$$

Here we directly reused the quadratic form in the IPC friction model (Equation 3) to ensure that f_t is always nonnegative. The tangential adhesion force first reaches its maximum value 1 at $y = \epsilon_a h$ and then decreases to 0 as tangential displacement increases. Together with $\lambda_{a,k}$, the maximum tangential adhesion force is the same as it is in the normal direction when $\mu_a = 1$, which also poses μ_a as an intuitively adjustable ratio for realizing different adhesive behaviors. As for ϵ_a, we can set it to the same value of ϵ_v.

The tangential adhesion model damps sliding while still permitting. Combining both the IPC friction and our tangential adhesion model then provides a tangential force-displacement relation consistent with the RCC model (see Figure 9). Now that $\lambda_{a,k}$ is constant per contact pair, with the tangent operator T_k for computing $\mathbf{u}_k$ temporally unvaried during the nonlinear optimization (Equation 1), we can similarly integrate the tangential adhesion forces to obtain an augmented potential energy $P_t(\mathbf{x}) = \sum_k (\mu \hat{\lambda}_k f_0(\|\hat{\mathbf{u}}_k\|) + \mu_a \lambda_{a,k} f_{t0}(\|\hat{\mathbf{u}}_k\|))$ with $f'_{t0}(y) = f_t(y)$ (note that the area weighting is inside λ). By performing fixed-point iterations that alternate between the nonlinear optimization and tangent variable updates, the solution with fully implicit tangential forces can be achieved.

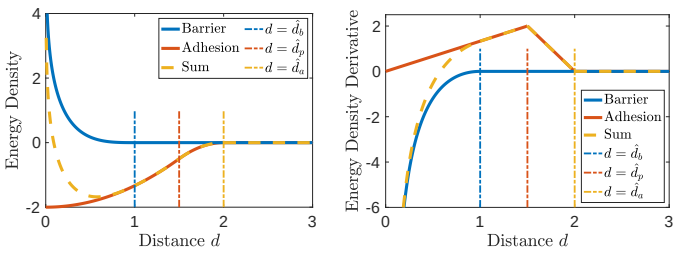

Fig. 7. **Normal Adhesion.** Plots of energy density and its derivative of our normal direction adhesive contact model. Here, we choose $\hat{d}_b = 1$, $\hat{d}_p = 1.5$, and $\hat{d}_a = 2$ for clear illustration.

5 Evaluation

We follow [46] to apply the projected Newton (PN) method with the filter-line-search scheme for solving the time-stepping optimization (Equation 1). In each PN iteration, Hessian matrices of the barrier, friction, adhesion, and elasticity potentials are first computed and projected to a close-by symmetric positive-definite (SPD) form per local stencil by clamping its negative eigenvalues to 0. Then, a search direction is computed by solving a linear system constructed with the gradient and the projected Hessian of the Incremental Potential. Next, we apply the additive continuous collision detection (ACCD) method from [31] to compute a large feasible step size to start the backtracking line search, which together ensures non-interpenetration and global convergence.

We implemented our system based on the Eigen linear algebra library [47], and parallelized our computations with Intel TBB. Our sparse linear systems are solved in parallel as well, with CHOLMOD [48] compiled using MKL BLAS and LAPACK for high efficiency. Note that we follow IPC to directly use squared distances as the input variables for both the barrier function $b(\cdot)$ and the normal adhesion energy density $a(\cdot)$ to avoid possible numerical instabilities introduced by taking the square root. This changes the expression of p, λ, and a_2 as extra chain rules will need to be applied.

In the remainder of this section, we start with an ablation study comparing directly applying RCC to IPC and our method (Section 5.1), followed by comparison to LCP-based method (Section 5.2). Then several examples are exhibited to validate our capability on capturing complex and realistic behaviors (Section 5.3 – 5.5). Finally, we demonstrate the versatility of our method by showing an additional set of complex examples with detailed analysis of the timing performance (Section 5.6). All of our experiments are running on a desktop with a 12-core Intel i9-10920X CPU at 3.50 GHz. The statistics are listed in Table 1. Following IPC, we, in practice, directly solve for the solution with semi-implicit tangential adhesive contact forces without performing more

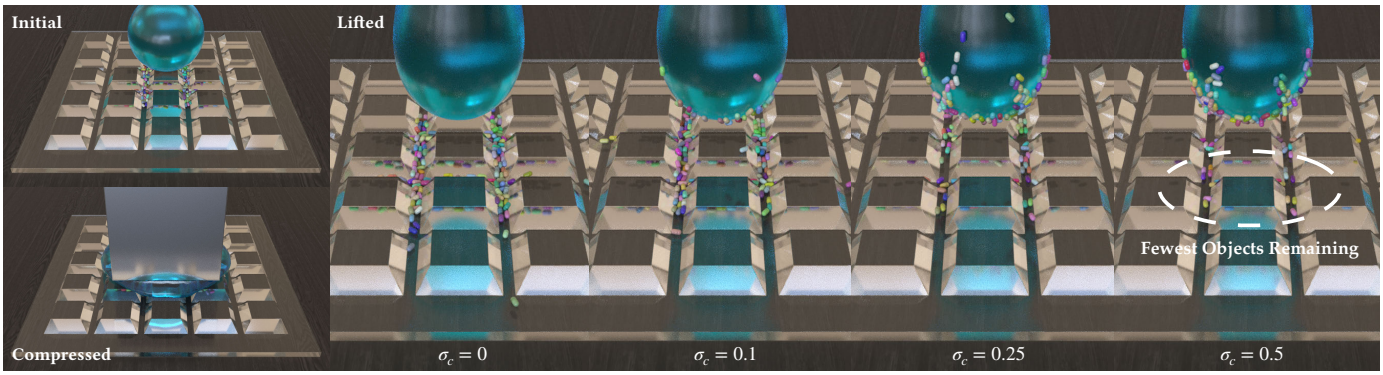

Fig. 8. **Cleaning Gel.** Our adhesion model is applicable to materials with various stiffnesses, including this extremely soft jello which can clean up tiny objects from small gaps. By setting the critical strain, ε_c, all the way from 0 (no adhesion) to 0.5, we can simulate the gel with different adhesion strength in a controllable way.

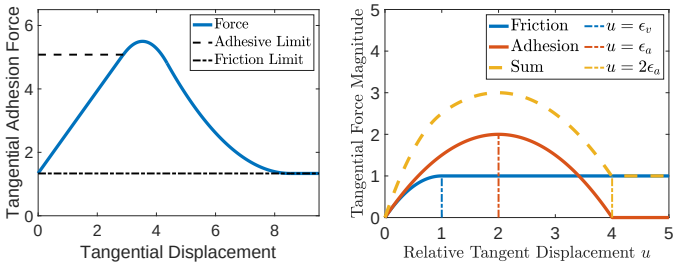

Fig. 9. **Tangential Adhesion.** Left: plot of the RCC tangential adhesion force w.r.t. tangential displacement [6]. Right: the force-displacement curve of our tangent direction adhesive contact model. Here we choose $\epsilon_v = 1$ and $\epsilon_a = 2$ for clear illustration.

fixed-point-iterations. This can already provide visually high-quality results. Please see [46] for further details.

5.1 Ablation Studies

Our experiments begin with ablation studies to demonstrate that, with only two user parameters (ε_c and μ_a) exposed, our adhesion model can effectively capture various adhesive effects. We further demonstrate that the distance thresholds do not have a significant impact on physical behaviors.

5.1.1 Adhesion Model

Here, we compare against the direct application of RCC in IPC to our variational model that captures the constitutive relation solely based on displacements. For simplicity, we will refer to them as *RCC* and *our method*.

We run an example using both methods to achieve similar adhesive behaviors and then compare the timing performance and the experience of parameter setting. In this example, we throw a bunch of sticky toys onto a fridge door. We want to capture versatile behaviors such that some of the toys stick on the fridge, while others fall down onto the ground. The results show that, with our target adhesive behaviors similarly achieved by the two methods (Figure 10), their timing performance is comparable (0.92 v.s. 0.88 min/step), while our method makes scene setup much more convenient by exposing only two parameters.

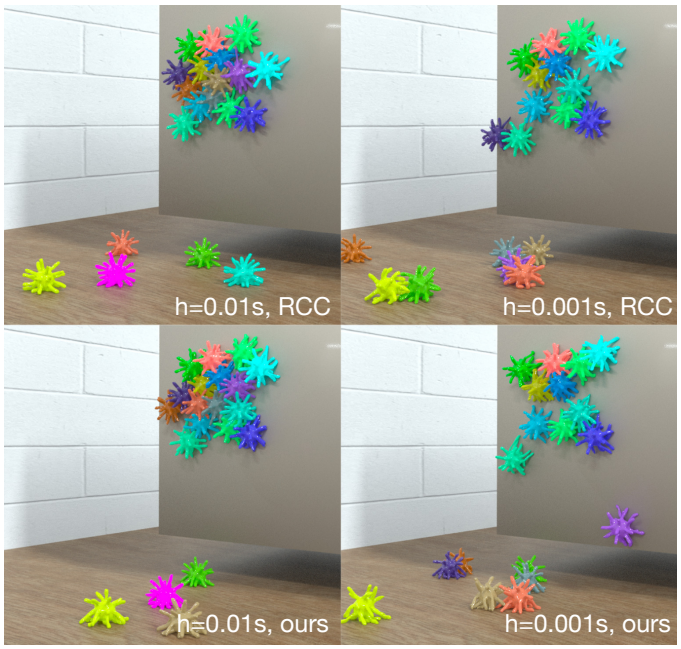

Fig. 10. **Sticky Toys.** Under gravity, friction, adhesion and elasticity, a total of 20 complex sticky toys are thrown onto a fridge door and bounce around. Here, when achieving similar adhesive behaviors, our method (bottom) has similar timing performance but fewer parameters to tune compared to RCC (top). With less numerical damping under smaller time step sizes (right), there are slightly fewer toys sticking to the fridge.

Finding a suitable set of RCC parameters that are stable and devoid of artifacts has been a laborious process; we even observed some nonphysical behaviors in the results if the six parameters are not all properly set. This issue might be exacerbated by simulating with large time step sizes ($h = 0.01s$), which makes the time-split adhesion intensity evolution prone to temporal discretization errors.

To provide further insights, we conducted additional experiments utilizing the identical simulation settings except with varying time step sizes $h = 0.01s$ (Figure 10 left) and $h = 0.001s$ (Figure 10 right). We observe that the overall animation is more dynamic with smaller time step sizes, resulting in slightly fewer toys sticking to the fridge. In

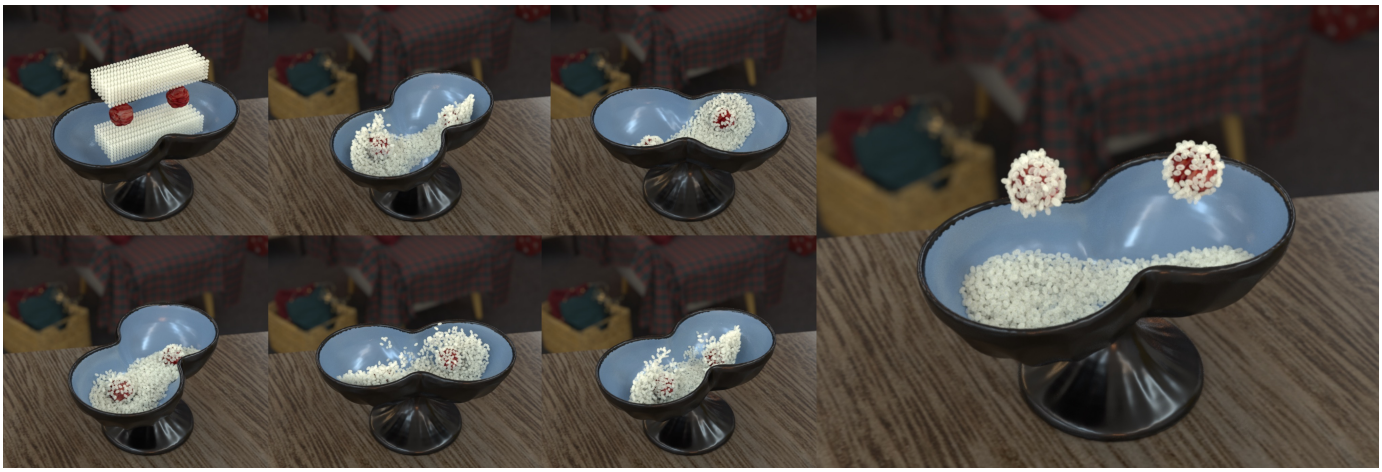

Fig. 11. **Making Meatballs.** Here, we selectively model adhesion only between the meatballs and the sticky rice grains to cook a traditional Chinese dish. As we shake the container after dropping the meatball and rice (left 6 images), the rice uniformly covers the meatball as shown on the right.

TABLE 1
Simulation Statistics. All experiments were performed on a 12-core Intel i9-10920X CPU. Scenes with a more frequently varied and/or larger set of active contact pairs tend to take more Newton iterations and, accordingly, have longer simulation times. *Here the Young's modulus Y are used for calculating the adhesion stiffness a_2. In the first four scenes, the values are from the sticky rice, spider, and Armadillo respectively.

Example	min/step	contacts/step	iter/step	h (s)	# nodes	Y (Pa)*	ε_c	μ_a
(Fig. 3) Sushi	1.07	60.5K	55.7	0.04	31K	4e5	0.05	1.0
(Fig. 11) Meatball	1.40	35.7K	32.6	0.04	53K	4e5	0.05	1.0
(Fig. 1) Spider Web	2.45	1.5K	58.1	0.01	4K	1e4	3.4	0.15
(Fig. 4) Tape	1.44	93.3K	24.2	0.02	46K	1e3	0.5	1.0
(Fig. 10) Sticky Toys	0.92	1.3K	42.6	0.01	23K	1e5	0.7	0.0
(Fig. 2) Wax	2.69	38.7K	54.8	0.01	22K	1e4	0.08	1.0
(Fig. 8) Cleaning Gel	0.15	7.0K	20.8	0.01	13K	4e3	0.5	1.0
(Fig. 6) Chips Bag	0.78	121.9K	22.8	0.01	31K	1e5	0.002	1.0

contrast, larger time step sizes generate more numerical damping and result in more toys sticking to the fridge for both RCC and our model. Notably, the results were consistent across both methods, and our adhesion model demonstrated similar effects to RCC. In the rest of this subsection, we will concentrate on the evaluation of our variational model.

5.1.2 Distance Threshold

The IPC model includes a barrier activation threshold $\hat{d}_b$, while our adhesion model introduces two additional parameters, $\hat{d}_p$ and $\hat{d}_a$, for adhesion activation. These parameters are crucial for achieving fast convergence. When assigned values extremely close to each other or too near to 0, they may result in floating point errors and also make the problem unnecessarily ill-conditioned.

To investigate the effects of these distance thresholds on the physical behaviors, we first maintain the relative magnitudes between these thresholds by setting $\hat{d}_b = \hat{d}_p = 0.5\hat{d}_a$ and scale them down by $0.1\times$ and $0.01\times$ to test the cleaning gel simulation with $\hat{d}_a = 10^{-3}, 10^{-4}, 10^{-5}$ (Figure 12 left three). Next, we keep $\hat{d}_b = 0.25\hat{d}_a$ and $\hat{d}_a$ unchanged and introduce a scaling factor s_p for $\hat{d}_p = s_p\hat{d}_a$. We test s_p for three values: $0.25, 0.5, 0.75$ (Figure 12 right three). For all these six sets of parameters, the results consistently exhibit similar adhesive effects when evaluating the quantity of dust pieces sticking to the gel.

The outcome of these experiments suggests that altering distance thresholds do not have a significant impact on the adhesive behaviors. Therefore, we fix $\hat{d}_b = \hat{d}_p = 0.5\hat{d}_a$ as the default option in practice and allow their absolute values to comply with $\hat{d}_b$, the IPC parameter, to accommodate varying mesh resolutions and dimensions.

5.2 Comparison to LCP-based Method

Gascon et al. [5] applied a constraint-based method to simulate adhesive contact. They followed [49] to define the contact constraints and elastodynamics and formulated linear complementarity problems (LCP) where contact, friction, and adhesion are treated as distinct constraint types. In comparison, we use conservative forces to approximate these behaviors, thereby transforming the implicit time integration into unconstrained optimizations.

To compare our method with Gascon et al. [5], we implemented an LCP solver in our simulation framework and applied it to handle the constraints of contact, friction, and adhesion. We set up a scene by fixing an adhesive square cloth (Figure 13) at its top, twisting it by rotating its bottom

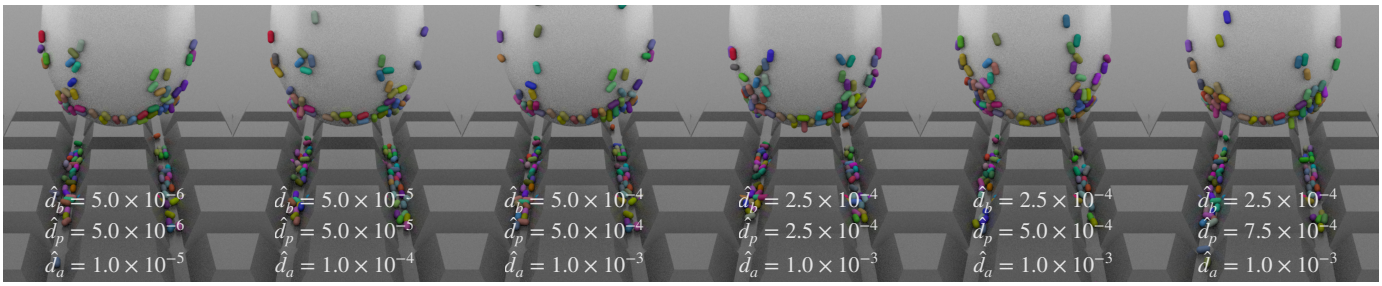

Fig. 12. **Comparisions with Different Distance Thresholds.** We simulate the cleaning gel example (Figure 8) with varying $\hat{d}_a$ (left three, fixing $\hat{d}_b = \hat{d}_p = 0.5\hat{d}_a$) and varying $\hat{d}_p$ (right three, fixing $\hat{d}_b = 0.25\hat{d}_a$ and $\hat{d}_a$). As similar adhesive effects are achieved, we conclude that $\hat{d}_p$ and $\hat{d}_a$ exert little influence on the physical behaviors when set in a reasonable range.

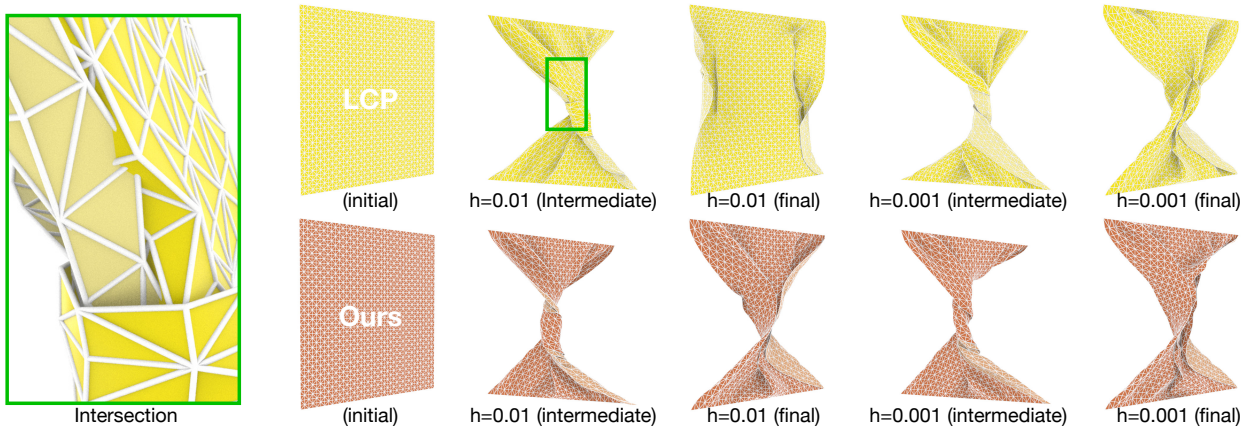

Fig. 13. **Comparison to Gascon et al.** We roll an adhesive thin sheet and subsequently unroll. The upper row, highlighted in yellow, illustrates the initial, intermediate, and final states when employing constraint-based methods with two distinct time step sizes $h = 0.01s$ and $h = 0.001s$. The lower row in orange displays the results of our approach under the same settings. When simulation gets challenging at large time step sizes, constraint-based methods are prone to interpenetration issues.

side in two rounds, and then rotating it backwards to its original configuration. Around the center area, the fabric will stick together and be pulled away later. Eventually, some portions of the cloth remain adhered. We simulate this scene with two time step sizes, $h = 0.01s$ and $h = 0.001s$, for both the LCP method and our approach. In general, a larger time step size results in vertices traveling longer distances, causing adhesive contact states to change more rapidly and become increasingly challenging. For smaller time step sizes, the animation sequences for both methods are similar. However, with larger time step sizes, penetration artifact occurs in the constraint-based method, causing the twisting knot to deviate from the central location and leading to a different final pose. As pointed out in [1] and [5], this issue is not unusual in constraint-based contact approaches regardless of the adhesion models being used. It arises from the absence of theoretical convergence guarantees for LCP and errors in its constraint linearization.

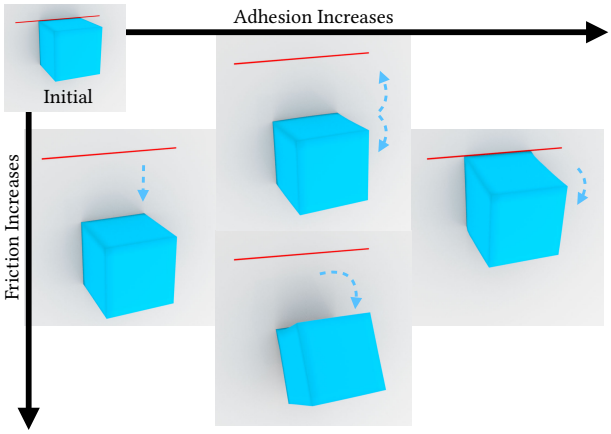

Fig. 14. **Tangential Adhesion v.s. Friction.** We simulate a cube sliding on or detaching from a wall with different tangential adhesion and friction coefficients. The behaviors intricately vary between different setups.

5.3 Adhesion v.s. Friction

Here, we design a simple example to study the intricate behaviors of mixed tangential adhesion and frictional effects. We place a $1m$-wide cube on a wall with an initial distance where the net force in the normal direction between them is 0 (Figure 14 top left). Gravity is set to $-9.81m/s^2$ in the vertical direction.

Without adhesion, no matter how large the friction coefficient is, the cube will slide down along the wall as if in free fall, as there are neither normal nor tangential contact forces (Figure 14 left). However, with large adhesion, no matter what the friction coefficient is, the cube will stick to the wall (Figure 14 right).

With small adhesion, the behavior becomes interesting.

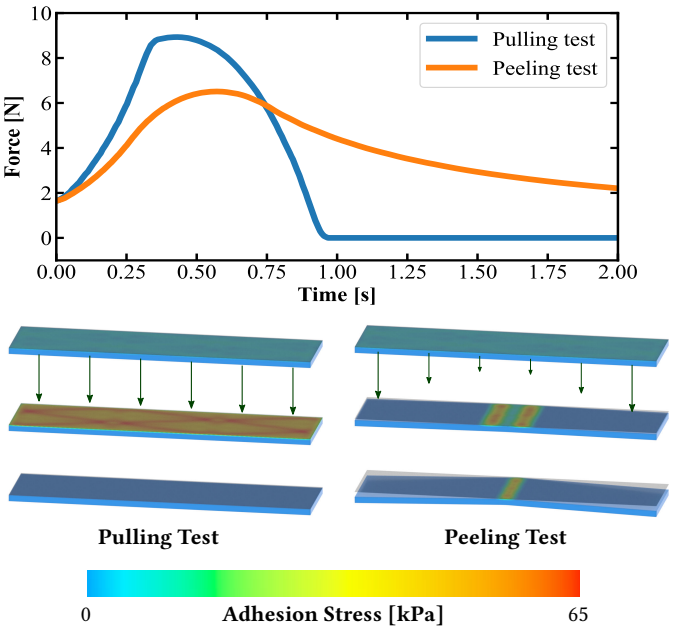

Fig. 15. **Comparison between two debonding processes.** We apply uniformly (bottom left) and linearly (bottom right) distributed loads to separate two adhesive plates initially stacked together with a gap of $0.25\hat{d}_p$. Plotting the total adhesion force w.r.t time (top), we clearly observe the bonding/debonding process is consistent with that of RCC (Figure 5).

If the friction coefficient is 0, the tangential adhesion force at the interface and the gravity force on the whole cube together form a torque, causing the cube to start to bend. Since adhesion is not sufficiently large, gravity quickly debonds the adhesion in the tangential direction and instigates the cube's downward slide accompanied by vertical vibrations. The cube remains attached to the wall due to normal adhesion (Figure 14 middle top). If the friction coefficient is large, similarly, under the combined effect of tangential adhesion and gravity, the cube will start to bend. However, as the cube bends, its left-bottom part is pushed inward, resulting in a normal contact force and thus large friction forces . Adhesion, however, remains insufficient, allowing gravity to debond it quickly. Ultimately, the right-top pointing frictional contact forces exerted at the left-bottom of the cube act like a support, causing the normal adhesion to debond first, making the cube rotate and finally detach from the wall (Figure 14 middle bottom).

5.4 Debonding

We perform two canonical tests, the parallel pulling and the peeling of two adhesive plates (Figure 15), inspired by [50], to validate that our simplified model can still capture the bonding/debonding process described by the RCC model.

In the parallel pulling experiment (Figure 15, bottom left), two plates are initially stacked with a gap of $0.25\hat{d}_p$. Since their distance is within the active region $(0, \hat{d}_a)$ of adhesion, bonding immediately occurs. We load the lower plate with uniformly distributed downward pulling forces whose magnitudes linearly increase with time until the plates detach. From the plot of total adhesion force w.r.t. time (Figure 15, top), we can see that the adhesion force first increases as distance increases until it reaches a peak, which corresponds to $d = \hat{d}_p$. Then, as the load keeps increasing, the gap also increases, and debonding happens with the adhesion force dropping all the way down to 0.

In the peeling experiment (Figure 15, bottom right), with the same initial geometric setting, we instead distribute the load linearly in the x-direction w.r.t the distance to the plate center. This different force distribution triggers a progressive debonding process starting from the left and right ends of the plate all the way to the center, which is clearly visualized by the stress profile. This progressive debonding behavior also results in a lower peak of the total adhesion force (Figure 15, top) comparing to the pulling test, where debonding occurs simultaneously.

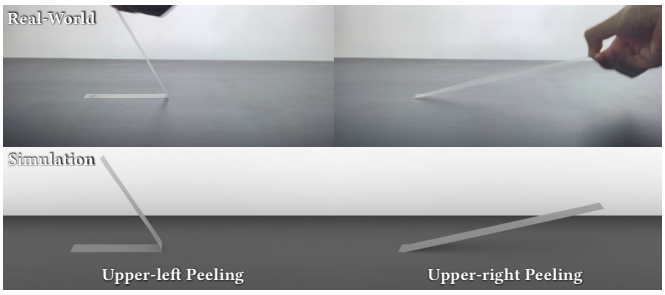

Fig. 16. **Peeling Tapes off a Desk.** With our adhesion model, our simulation well-matches video capture of real-world experiments on peeling tapes off a desk towards different directions.

5.5 Real-World Experiments

To further validate our method with real-world experiments, we stick a strip of adhesive tape on a desk surface, and peel the tape from its right end towards different directions.

When peeling towards the upper-left direction (Figure 16, left), the tape progressively detaches the desk from right to left, where the detached tape is straight under mild tension and it forms a right angle with the unpeeled part. When peeling towards the upper-right direction (Figure 16, right), the detachment happens rapidly throughout the whole strip under large tension right after the right end travels just a short distance. After the left end of the tape is finally detached, the tape quickly rolls due to inertia effects. From the side-by-side comparison, we observe that our simulation (Figure 16, bottom) well-matches the video footage of our real-world experiment (Figure 16, top).

5.6 Performance

To evaluate the performance of our method, we simulate more examples with sticky interactions that are commonly seen in our daily life, including rolling sushi (Figure 3), making sticky rice balls (Figure 11), taping the Armadillo (Figure 4), opening chips bag (Figure 6), sealing wax on an envelope (Figure 2), cleaning keyboard (Figure 8), and spider webs (Figure 1). With straightforward parameter setting, our method robustly simulated all these scenes without any interpenetrations, capturing intricate adhesive behaviors.

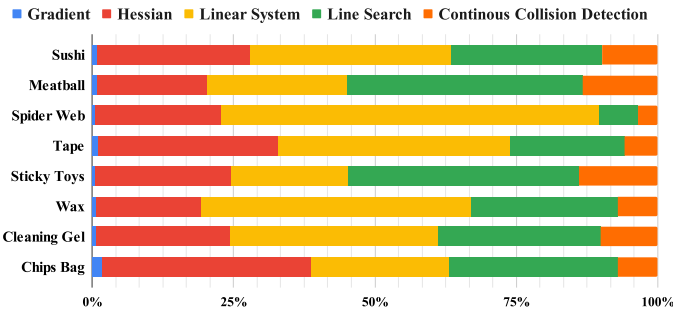

Fig. 17. **Timing Breakdown.** Here, the Hessian timing includes both the computation and the SPD projection; the line search timing is dominated by finding all active contact pairs. Hessian-related computations (red and yellow) and spatial searches (green and orange) are the two main bottlenecks of our method.

5.6.1 *Timing Breakdown*

In Figure 17, we demonstrate the timing breakdowns of all examples. Here, the proportion of time spent on each of the main components is plotted. Note that computing the Hessian matrix with SPD projections and then solving the linear system by direct factorization take most of the time for nearly all examples. The remaining bottlenecks comprise CCD and line search wherein the barrier energy is evaluated in each backtracking. Improving Hessian-related computations is non-trivial. Although matrix-free Krylov solvers can be an attractive candidate, without effective preconditioners, they may require a large number of iterations to solve our stiff barrier systems, which won't significantly improve the efficiency. Fortunately, GPU acceleration on spatial searches is a well-explored direction, and there are promising candidates that can be applied in our method. We leave investigating performance accelerations on our method as a meaningful future work.

5.6.2 *Newton Solver Configuration*

Based on our unconstrained formulation of the adhesive contact simulation, we can directly use the Newton solver, therefore benefiting from a second-order convergence rate. We set the convergence criterion as the infinite norm of the search direction divided by time step size h going below a certain threshold (e.g., 0.01 for most examples). Additionally, we demonstrate that within a reasonable range, different distance thresholds do not substantially affect solver convergence (Figure 18).

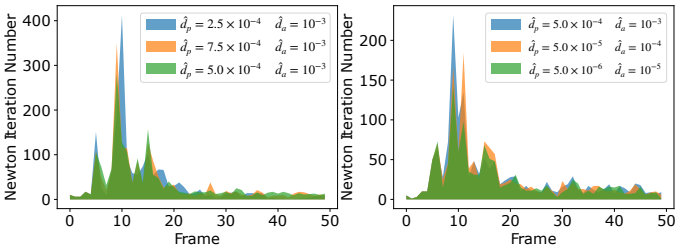

Fig. 18. **Newton Iteration Count per Frame.** Here we show the Newton iteration count per frame of the cleaning gel simulation in Figure 12 with different distance thresholds.

5.6.3 *Different Adhesion Strength*

Here we analyze the impact of adhesion strength on simulation performance by simulating the cleaning gel example with different critical strain ε_c (Figure 8). With larger adhesion, more dust objects are removed from the keyboard and stick to the gel, generating more contacts and making the Incremental Potential more challenging to minimize as it becomes less convex and smooth. As a result, the required PN iterations to converge under the same criteria increase (Figure 19, right). However, the timing is not strictly increasing with the adhesion strength (Figure 19, left). In the $\varepsilon_c = 0.1$ case, we observed that the spatial hash data structure used in IPC was providing suboptimal performance as the dust objects occasionally fall out of the keyboard, increasing the bounding box of the scene together with the hash cell size, which is a sensitive attribute for achieving the best performance. We leave utilizing more adaptive data structures like the Bounding Box Hierarchy (BVH) for improving the spatial search for future work.

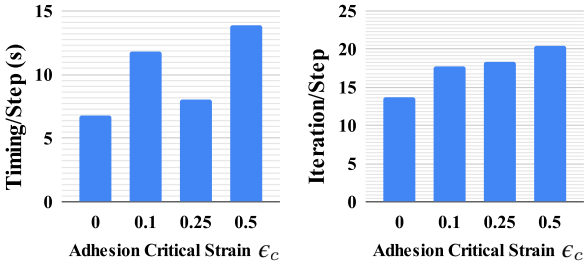

Fig. 19. **Performance under Different Adhesion Strength.** Here we demonstrate the timing and iterations per time step for the cleaning gel example with different adhesion strengths (Figure 8).

6 Conclusion and Future Work

We presented a distance-based variational adhesive frictional contact model for the animation of sticky elastoplastic solids. Our model can be conveniently deployed in the Incremental Potential Contact (IPC) simulator, allowing intricate adhesion effects coupled with large deformation to be robustly simulated with non-penetration guarantees, bringing important dynamical details to computer graphics in a reliable way. By directly modeling the constitutive relation between adhesion forces and displacements, our model enables controllable simulation of versatile adhesive behaviors with only two physical parameters.

In this study, we employ the combination of RCC and IPC as a starting point, but we advocate for our approach, which is more practical and stable. Thus, our variational model is produced, which enables simulations of adhesion with large timestep sizes. It only approximates RCC and is hence less physically precise and expressive, yet we greatly favor its two key benefits: (1) Only 2 intuitive parameters are needed. (2) Incorporating the adhesion intensity into the potential energy permits efficient simulation at large timestep sizes without artifacts, and this is true even with careless parameter selections. Note that when RCC utilizes inadequately selected parameters, the simulation may still remain stable due to the heuristic clamping of β_k. This conceals the existence of exploded numerical solutions to

the ODE for β_k and can lead to artifacts. The further investigation of such behaviors and the development of a more stable and user-friendly technique for simulating the full spectrum RCC model within or outside the IPC framework is left to future research.

Similar to IPC friction, although our method guarantees convergence to the solution with semi-implicit tangential forces, the fixed-point iterations in the outer loop can only converge when the initial point is sufficiently close to the fully-implicit solution. It will be theoretically valuable to further analyze the convergence property of this iterative strategy. In addition, although our model can resolve complex and intricate adhesive behaviors in various animation examples, the simplifications may restrict the expressiveness of the original RCC model. There is also plenty of room for improvement in the timing performance of our method. We can explore GPU accelerations on the spatial search, and also more efficient and scalable (non-)linear solvers suitable for stiff barrier systems. Extending our model for adhesive solid-fluid interactions based on IPC will be another impactful direction.

REFERENCES

[1] M. Li, Z. Ferguson, T. Schneider, T. Langlois, D. Zorin, D. Panozzo, C. Jiang, and D. M. Kaufman, "Incremental potential contact: Intersection-and inversion-free, large-deformation dynamics," *ACM transactions on graphics*, 2020.

[2] R. Bridson, R. Fedkiw, and J. Anderson, "Robust treatment of collisions, contact and friction for cloth animation," in *Proceedings of the 29th annual conference on Computer graphics and interactive techniques*, 2002, pp. 594–603.

[3] J. Li, G. Daviet, R. Narain, F. Bertails-Descoubes, M. Overby, G. E. Brown, and L. Boissieux, "An implicit frictional contact solver for adaptive cloth simulation," *ACM Transactions on Graphics (TOG)*, vol. 37, no. 4, pp. 1–15, 2018.

[4] M. Ly, J. Jouve, L. Boissieux, and F. Bertails-Descoubes, "Projective dynamics with dry frictional contact," *ACM Transactions on Graphics (TOG)*, vol. 39, no. 4, pp. 57–1, 2020.

[5] J. Gascón, J. S. Zurdo, and M. A. Otaduy, "Constraint-based simulation of adhesive contact," in *Symposium on Computer Animation*, 2010, pp. 39–44.

[6] M. Raous, L. Cangémi, and M. Cocu, "A consistent model coupling adhesion, friction, and unilateral contact," *Computer methods in applied mechanics and engineering*, vol. 177, no. 3-4, pp. 383–399, 1999.

[7] X. Li, M. Li, and C. Jiang, "Energetically consistent inelasticity for optimization time integration," *ACM Trans. Graph. (SIGGRAPH)*, vol. 41, no. 4, 2022.

[8] J. Israelachvili, S. Giasson, T. Kuhl, C. Drummond, A. Berman, G. Luengo, J.-M. Pan, M. Heuberger, W. Ducker, and N. Alcantar, "Some fundamental differences in the adhesion and friction of rough versus smooth surfaces," in *Tribology Series*. Elsevier, 2000, vol. 38, pp. 3–12.

[9] K. L. Johnson, *Contact mechanics*. Cambridge university press, 1987.

[10] B. V. Derjaguin, V. M. Muller, and Y. P. Toporov, "Effect of contact deformations on the adhesion of particles," *Journal of Colloid and interface science*, vol. 53, no. 2, pp. 314–326, 1975.

[11] J. E. Lennard-Jones, "Cohesion," *Proceedings of the Physical Society (1926-1948)*, vol. 43, no. 5, p. 461, 1931.

[12] N. Yu and A. A. Polycarpou, "Adhesive contact based on the lennard–jones potential: a correction to the value of the equilibrium distance as used in the potential," *Journal of Colloid and Interface Science*, vol. 278, no. 2, pp. 428–435, 2004.

[13] M. Paggi and J. Reinoso, "A variational approach with embedded roughness for adhesive contact problems," *Mechanics of Advanced Materials and Structures*, vol. 27, no. 20, pp. 1731–1747, 2020.

[14] L. Hu, Y. Cong, and Z.-Q. Feng, "Simulation of adhesive frictional contact of soft materials by bi-potential method," in *14th WCCM-ECCOMAS Congress*. CIMNE, 2021.

[15] L. Hu, Y. Cong, P. Joli, and Z.-Q. Feng, "A bi-potential contact formulation for recoverable adhesion between soft bodies based on the rcc interface model," *Computer Methods in Applied Mechanics and Engineering*, vol. 390, p. 114478, 2022.

[16] S. Clavet, P. Beaudoin, and P. Poulin, "Particle-based viscoelastic fluid simulation," in *Proceedings of the 2005 ACM SIGGRAPH/Eurographics symposium on Computer animation*, 2005, pp. 219–228.

[17] M. Bergou, B. Audoly, E. Vouga, M. Wardetzky, and E. Grinspun, "Discrete viscous threads," *ACM Transactions on graphics (TOG)*, vol. 29, no. 4, pp. 1–10, 2010.

[18] C. Batty, A. Uribe, B. Audoly, and E. Grinspun, "Discrete viscous sheets," *ACM Transactions on Graphics (TOG)*, vol. 31, no. 4, pp. 1–7, 2012.

[19] H. Schechter and R. Bridson, "Ghost sph for animating water," *ACM Transactions on Graphics (TOG)*, vol. 31, no. 4, pp. 1–8, 2012.

[20] N. Akinci, G. Akinci, and M. Teschner, "Versatile surface tension and adhesion for sph fluids," *ACM Transactions on Graphics (TOG)*, vol. 32, no. 6, pp. 1–8, 2013.

[21] Y. Fei, H. T. Maia, C. Batty, C. Zheng, and E. Grinspun, "A multi-scale model for simulating liquid-hair interactions," *ACM Transactions on Graphics (TOG)*, vol. 36, no. 4, pp. 1–17, 2017.

[22] Y. Fei, C. Batty, E. Grinspun, and C. Zheng, "A multi-scale model for simulating liquid-fabric interactions," *ACM Transactions on Graphics (TOG)*, vol. 37, no. 4, pp. 1–16, 2018.

[23] ——, "A multi-scale model for coupling strands with shear-dependent liquid," *ACM Transactions on Graphics (TOG)*, vol. 38, no. 6, pp. 1–20, 2019.

[24] M. Leach and S. Maddock, "Physically-based sticky lips," in *Proceedings of the Conference on Computer Graphics & Visual Computing*, 2018, pp. 51–59.

[25] J. Nocedal and S. J. Wright, *Numerical optimization*. Springer, 1999.

[26] P. Christensen, A. Klarbring, J.-S. Pang, and N. Strömberg, "Formulation and comparison of algorithms for frictional contact problems," *International Journal for Numerical Methods in Engineering*, vol. 42, no. 1, pp. 145–173, 1998.

[27] T. Belytschko, W. Liu, and B. Moran, *Nonlinear Finite Elements for Continua and Structures*. John Wiley & Sons, Ltd, 2000.

[28] G. Kloosterman, R. M. van Damme, A. H. van den Boogaard, and J. Huetink, "A geometrical-based contact algorithm using a barrier method," *International Journal for Numerical Methods in Engineering*, vol. 51, no. 7, pp. 865–882, 2001.

[29] J. M. Kaldor, D. L. James, and S. Marschner, "Simulating knitted cloth at the yarn level," in *ACM SIGGRAPH 2008 papers*, 2008, pp. 1–9.

[30] D. Harmon, E. Vouga, B. Smith, R. Tamstorf, and E. Grinspun, "Asynchronous contact mechanics," in *ACM SIGGRAPH 2009 papers*, 2009, pp. 1–12.

[31] M. Li, D. M. Kaufman, and C. Jiang, "Codimensional incremental potential contact," *ACM Trans. Graph. (SIGGRAPH)*, vol. 40, no. 4, 2021.

[32] L. Lan, Y. Yang, D. Kaufman, J. Yao, M. Li, and C. Jiang, "Medial ipc: accelerated incremental potential contact with medial elastics," *ACM Transactions on Graphics (TOG)*, vol. 40, no. 4, pp. 1–16, 2021.

[33] Z. Ferguson, M. Li, T. Schneider, F. Gil-Ureta, T. Langlois, C. Jiang, D. Zorin, D. M. Kaufman, and D. Panozzo, "Intersection-free rigid body dynamics," *ACM Transactions on Graphics (SIGGRAPH)*, vol. 40, no. 4, 2021.

[34] L. Lan, D. M. Kaufman, M. Li, C. Jiang, and Y. Yang, "Affine body dynamics: Fast, stable & intersection-free simulation of stiff materials," *ACM Trans. Graph. (SIGGRAPH)*, vol. 41, no. 4, 2022.

[35] Y. Chen, M. Li, L. Lan, H. Su, Y. Yang, and C. Jiang, "A unified newton barrier method for multibody dynamics," *ACM Trans. Graph. (SIGGRAPH)*, vol. 41, no. 4, 2022.

[36] L. Lan, G. Ma, Y. Yang, C. Zheng, M. Li, and C. Jiang, "Penetration-free projective dynamics on the gpu," *ACM Trans. Graph. (SIGGRAPH)*, vol. 41, no. 4, 2022.

[37] Y. Zhao, J. Choo, Y. Jiang, M. Li, C. Jiang, and K. Soga, "A barrier method for frictional contact on embedded interfaces," *Computer Methods in Applied Mechanics and Engineering*, vol. 393, p. 114820, 2022.

[38] X. Li, Y. Fang, M. Li, and C. Jiang, "Bfemp: Interpenetration-free mpm–fem coupling with barrier contact," *Computer Methods in Applied Mechanics and Engineering*, p. 114350, 2021.

[39] Y. Jiang, Y. Zhao, C. E. Choi, and J. Choo, "Hybrid continuum-discrete simulation of granular impact dynamics," *arXiv preprint arXiv:2108.02080*, 2021.
[40] C. Schüller, L. Kavan, D. Panozzo, and O. Sorkine-Hornung, "Locally injective mappings," in *Computer Graphics Forum*, vol. 32, no. 5. Wiley Online Library, 2013, pp. 125–135.
[41] J. Smith and S. Schaefer, "Bijective parameterization with free boundaries," *ACM Transactions on Graphics (TOG)*, vol. 34, no. 4, pp. 1–9, 2015.
[42] Z. Jiang, S. Schaefer, and D. Panozzo, "Simplicial complex augmentation framework for bijective maps," *ACM Transactions on Graphics*, vol. 36, no. 6, 2017.
[43] Y. Fang, M. Li, C. Jiang, and D. M. Kaufman, "Guaranteed globally injective 3d deformation processing," *ACM Trans. Graph.(TOG)*, vol. 40, no. 4, 2021.
[44] M. Ortiz and L. Stainier, "The variational formulation of viscoplastic constitutive updates," *Computer methods in applied mechanics and engineering*, vol. 171, no. 3-4, pp. 419–444, 1999.
[45] M. Li, M. Gao, T. Langlois, C. Jiang, and D. M. Kaufman, "Decomposed optimization time integrator for large-step elastodynamics," *ACM Transactions on Graphics*, vol. 38, no. 4, 2019.
[46] M. Li, "Robust and accurate simulation of elastodynamics and contact," Ph.D. dissertation, University of Pennsylvania, 2020.
[47] G. Guennebaud, B. Jacob *et al.*, "Eigen v3," http://eigen.tuxfamily.org, 2010.
[48] Y. Chen, T. A. Davis, W. W. Hager, and S. Rajamanickam, "Algorithm 887: Cholmod, supernodal sparse cholesky factorization and update/downdate," *ACM Transactions on Mathematical Software (TOMS)*, vol. 35, no. 3, pp. 1–14, 2008.
[49] M. A. Otaduy, R. Tamstorf, D. Steinemann, and M. Gross, "Implicit contact handling for deformable objects," vol. 28, no. 2, 2009.
[50] H. Sönnerlind, "How to model adhesion and decohesion in comsol multiphysics," Jul 2016. [Online]. Available: https://www.comsol.com/blogs/how-to-model-adhesion-and-decohesion-in-comsol-multiphysics

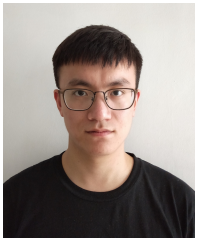

Yu Fang is a Ph.D. student majoring in Computer and Information Science at University of Pennsylvania. He is advised by Prof. Chenfanfu Jiang and is currently visiting UCLA. Yu graduated from Tsinghua University in 2018. His primary research interest is physically based simulation. Currently, Yu has been working on utilizing material point method (MPM) to simulate different phenomena and developing novel technology to accelerate existing simulation framework.

Minchen Li is an Assistant Professor in the CS department at Carnegie Mellon University. He was previously an Assistant Adjunct Professor of Mathematics at UCLA following his Ph.D. from the University of Pennsylvania. Minchen's Ph.D. dissertation, advised by Chenfanfu Jiang, is recognized by the 2021 ACM SIGGRAPH Outstanding Doctoral Dissertation Award for introducing the Incremental Potential Contact (IPC) method, which has led to a series of follow-up works in both academia and industry.

Yadi Cao is a Ph.D. student in Computer Science at UCLA, under the supervision of Prof. Chenfanfu Jiang and Prof. Demetri Terzopoulos. His primary research interest is optimizing large-scale machine learning, as well as the potential application of machine learning in the physical simulation, engineering design, and operation research. Yadi received his MASc in Mechanical Engineering from the University of British Columbia in 2018.

Xuan Li is a Ph.D. in Mathematics at UCLA, advised by Prof. Chenfanfu Jiang. Before that, he was a PhD student at Sig Lab, the University of Pennsylvania, working in the same group. Xuan's current research interests are physics-based simulation, ML-aided simulation and sim2real/real2sim applications. Xuan received his M.Sc. in Computer Science from the State University of New York at Stony Brook in 2020, and his B.Sc. in Mathematical Sciences from Tsinghua University (China) in 2017.

Joshuah Wolper is currently a postdoctoral researcher at UPenn MEAM studying methods to simulate thrombotic rupture, embolism, and fibrin fracture in collaboration with Professors John Bassani, Prashant Purolhit, and experts at the Perelman School of Medicine. As a past Harlan Stone Fellow at the University of Pennsylvania, Joshuah recently finished his PhD in Computer and Information Science advised by Professor Chenfanfu Jiang. His dissertation is Material Point Methods for Simulating Material Fracture.

Yin Yang is an associate professor with School of Computing, University of Utah. Yin received his Ph.D. from University of Texas at Dallas (with David Daniel fellowship). He is a recipient of the NSF CRII award (2015) and CAREER award (2019). Yin's research aims to develop efficient and customized computing methods for challenging problems in Graphics, Simulation, Machine Learning, Vision, Visualization, Robotics, Medicine, and many other applied areas.

Chenfanfu Jiang is an associate professor of Mathematics at UCLA. He obtained his Ph.D. degree in 2015 from UCLA co-advised by Demetri Terzopoulos and Joseph Teran. He is a recipient of the UCLA Edward K. Rice Outstanding Doctoral Student Award (2015) and NSF CAREER award (2020). He directs UCLA Multi-Physics Lagrangian-Eulerian Simulations Laboratory with projects spanning scientific computing, computer graphics, metaverse, computational mechanics, machine learning.